ORIGINAL PAPER

Numerical Simulation Study on Mechanical and Acoustic Emission Characteristics of Coal–Rock Combined Body Subjected to Cyclic Disturbing Loading

Huiqiang Duan · **Si Xiong** · **Weibo Yu**

Abstract In order to further study the mechanical properties of coal–rock combined body, the conventional uniaxial compression and cyclic disturbing loading tests were carried on it by numerical simulation method. The main conclusions are as follows: Under the same rock proportion, the strength and elastic modulus of sandstone–coal–sandstone (SCS) combined body in conventional uniaxial compression test are greater than that of mudstone–coal–mudstone (MCM) combined body; and their strength and elastic modulus increase exponentially with the increase of rock proportion. In the conventional uniaxial compression and cyclic disturbing loading tests, with the increase of rock proportion, the difference of stress–strain curve shape of SCS and MCM combined bodies increases, and the peak axial strain of SCS and MCM combined bodies shows the evolution characteristics of "first decreasing and then increasing". Under the same rock proportion, the strength of SCS combined body in cyclic disturbing loading test is greater than that of MCM combined body; and their strength increases exponentially with the increase of rock proportion. The cyclic disturbing loading has two effects on the combined bodies, namely: plastic softening and plastic strengthening effects. The mutual restriction and competition of these two effects will determine the strength of combined body. Under the same rock proportion, the maximum AE hit count of MCM combined body is greater than that of SCS combined body, and the maximum AE hit count of SCS and MCM combined bodies presents the characteristics of "big at both ends and small in the middle" with the increase of rock proportion.

Keywords Coal–rock combined body · Cyclic disturbing loading · Strength · Elastic modulus · Crack evolution · Acoustic emission

H. Duan (✉) · S. Xiong · W. Yu
School of Mining and Coal, Inner Mongolia University of Science and Technology, No. 7, Aerding Street, Kundulun District, Baotou City 014010, Inner Mongolia Autonomous Region, People's Republic of China
e-mail: duanhuiqiang11@163.com

S. Xiong
e-mail: 930106532@qq.com

W. Yu
e-mail: 1767506097@qq.com

1 Introduction

Various types of barrier coal pillars need to be designed in underground coal mine. The stability of these coal pillars do play an important role in safety production of coal mine. Once the collapse of these coal pillars will lead to very serious disasters. For example, In China, there occurred many rockburst, water-inrush and gas emission accidents caused by the instability of coal pillar (Li et al. 2020, 2021; Xin et al. 2021; He et al. 2021a; Luo et al. 2021; Gao et al. 2021). In the United States, more than 50

incidents of surface subsidence have been recorded for the instability of coal pillars (Yang et al. 2016). In South Africa, many coal pillars suddenly collapsed after many years, resulting in surface subsidence (Van der Merve 2006). Under normal circumstances, with the continuous increase of mining intensity, the disturbing stress triggered by mining and excavation activities increases. That is, the coal pillars collapse after undergoing the disturbing loads with multi-level stress amplitude. Actually, the essence of coal pillar instability is the embodiment of the instability of the "roof-coal pillar-floor" combined system, and the instability of any part in the system will cause the overall collapse. So, to study the mechanical properties of rock–coal–rock-typed combined body can better reveal the essential characteristics of coal pillar instability than only studying the instability of coal specimen.

Now, many scholars have made a lot of research on the mechanical properties of coal–rock combined body subjected to conventional compression loading, and achieved the rich research results. For example, some scholars have studied the strength of coal–rock combined body (Zhang et al. 2018; Chen et al. 2020). Some scholars have studied the energy evolution and distribution characteristics of coal–rock combined body (Yang et al. 2019, 2020; He et al. 2021b; Chen et al. 2021; Pan et al. 2021). Some scholars have studied the failure mechanism of coal–rock combined body (Chen et al. 2019; Gao et al. 2020; Liu et al. 2021). Lu et al. (2021) have studied the influence of loading rate on the failure characteristics of composite coal–rock specimens under quasi-static loading conditions. Xue et al. (2022) have studied the failure characteristics of coal–rock combined bodies based on acoustic emission signals. The above research results make us have a certain understanding of the mechanical properties of coal–rock combined body. But, there are few study on the mechanical properties of coal–rock combined body subjected to cyclic disturbing loading.

In reality, the coal and rock specimens can only suffer from one destructive test, but, the numerical simulation test has the advantages of repeatability (Chen et al. 2016). So, a reliable regularity can easily be obtained by numerical simulation method to study the influence of cyclic disturbing loading on the mechanical properties of coal–rock combined body. Based on this, this paper employs the numerical

simulation software of Particle Flow Code (PFC) to study this problem.

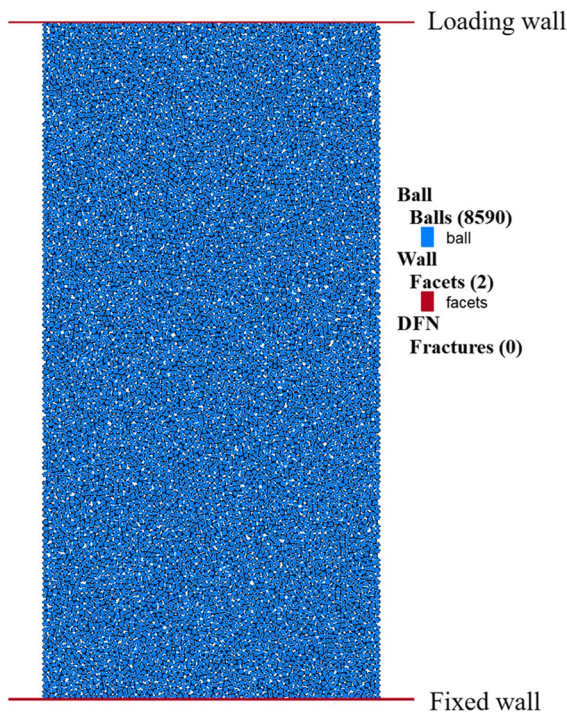## 2 Numerical Simulation Model and Meso-parameters

2.1 Model Establishment

In this paper, the PFC 2D software is employed. The established model width is 50 mm, and with a height of 100 mm. In the simulation test, the smaller the particle size, the more accurate the simulation results, but which also obviously reduces the computing efficiency. If the particle size is too large, the reliability of simulation results is very bad, and difficult to reflect the real mechanical properties of specimens. Therefore, in the numerical simulation test, it is necessary to make a trade-off between computing accuracy and efficiency to determine the reasonable number and size range of particles. The research achievements have shown that when the average particle size is less than 2.5% of the model minimum size, the better simulation results can be achieved (Zhang 2014). Through repeated debugging, the size range of particles in the model was determined to be from 0.32 mm to 0.49 mm, and there generated 8590 particles in all. The established model was shown in Fig. 1, the top wall is used for loading, and the bottom wall is fixed. The Linearpbond contact model is employed among particles, and the Linear contact model is employed between particles and walls.

2.2 Lab Test and Calibration of Meso-parameters

2.2.1 Lab Test

The big block of coal, mudstone and sandstone samples were from No. 16 upper coal seam of Yangcun Mine's No. 10602 coal face in Shandong, China. Three processes of slow drilling, cutting and grinding are adopted to process each sample into several standard cylindrical specimens with a diameter of 50 mm and a height of 100 mm, which is suggested by the International Society for Rock Mechanics (ISRM). The conventional uniaxial compression tests were conducted using the MTS815.02 rock-mechanics test system (MTS Systems Corporation, Eden Prairie, MN, U.S.A.) from China University of Mining
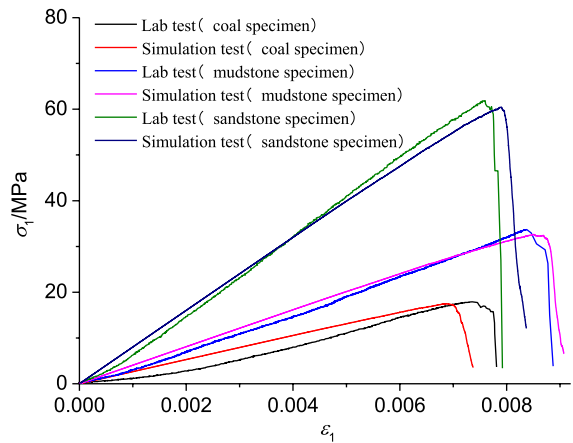
Fig. 1 Numerical model of basic specimen

Table 1 The parameters of the model

Model parameters	Coal specimen	Mudstone specimen	Sandstone specimen
Emod/Pa	2.2e9	3.1e9	6.0e9
kratio	15.0	10.0	11.0
pb_emod/Pa	1.9e9	2.8e9	5.8e9
pb_kratio	15.0	10.0	11.0
pb_ten/Pa	16.0e6	30.0e6	53.0e6
pb_coh/Pa	2.5e6	5.0e6	10.0e6
pb_fa	0.0	0.0	0.0
dp_nratio	0.8	0.8	0.8
dp_sratio	0.8	0.8	0.8
fric	0.4	0.4	0.4

Fig. 2 Comparison of simulation axial stress–strain curve and lab test curve on coal, mudstone and sandstone specimens

Table 2 Test results of coal specimen subjected to conventional uniaxial compression in lab and simulation tests

Test type	σ_C/MPa	ε_C/‰	E/MPa	μ
Lab test	17.898	7.355	2854.824	0.342
Simulation test	17.495	6.822	2633.014	0.311
Error/%	−2.252	−7.247	−7.770	−9.064

and Technology. The test was carried out using the displacement control mode with a loading rate of 0.003 mm/s.

2.2.2 Calibration of Meso-parameters

During the calibration of meso-parameters, it is required that the simulation stress–strain curve should coincide with the lab test curve, which needs to be determined by trial–error method (Mu et al. 2014; Liu et al. 2015). Meanwhile, There exist a sensitiveness of loading rate in the strength and deformation properties of rock. So, the conventional compression test with different loading rates is required in numerical simulation test to obtain the static whole process stress–strain curve corresponding to lab test. For the established model, through repeated tests, it is determined to be static loading process that when the loading rate is less than or equal to 0.05 m/s. The detailed numerical model parameters of coal, mudstone and sandstone specimens are shown in Table 1, the corresponding conventional uniaxial compression stress–strain curves of numerical simulation test and

lab test are shown in Fig. 2, and the corresponding test results are shown in Tables 2, 3 and 4.

In Fig. 2, the symbol "σ_1" represents the axial stress, and "ε_1" represents the axial strain. In Tables 2, 3 and 4, the symbol "σ_C" represents the peak strength, "ε_C" represents the peak axial strain

Table 3 Test results of mudstone specimen subjected to conventional uniaxial compression in lab and simulation tests

Test type	σ_C/MPa	ε_C/‰	E/MPa	μ
Lab test	33.703	8.368	3774.636	0.322
Simulation test	32.63	8.495	4042.909	0.295
Error/%	− 3.184	1.518	7.107	− 8.385

Table 4 Test results of sandstone specimen subjected to conventional uniaxial compression in lab and simulation tests

Test type	σ_C/MPa	ε_C/‰	E/MPa	μ
Lab test	61.859	7.598	8806.758	0.272
Simulation test	60.444	7.903	7998.269	0.256
Error/%	− 2.287	4.014	− 9.18	− 5.882

(refers to the axial strain corresponding to peak strength), "E" represents the elastic modulus in elastic phase, "μ" represents the Poission's ratio.
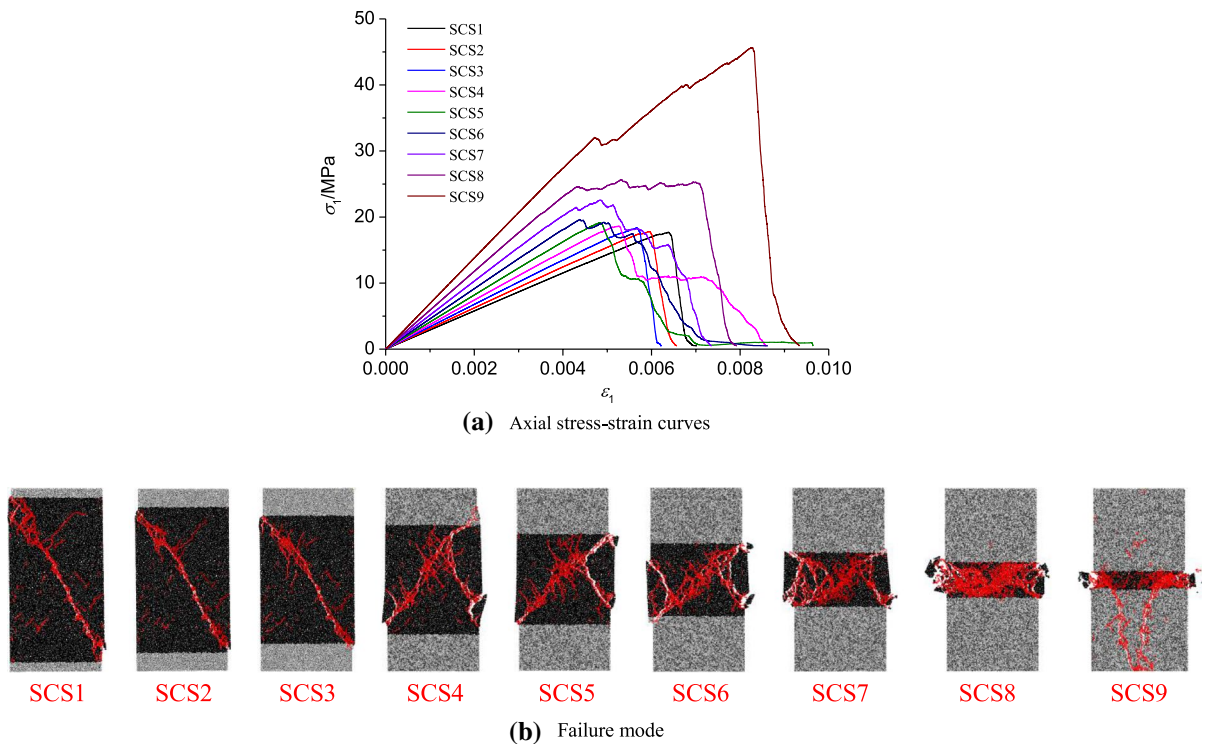
3 Mechanical Properties of Coal–Rock Combined Body in Conventional Uniaxial Compression Test

In order to study the mechanical properties of rock–coal–rock-typed combined body, the sandstone-coal-sandstone (SCS) and mudstone-coal-mudstone (MCM) combined bodies with the height of 100 mm and the diameter of 50 mm were designed. The specific combination scheme is shown in Table 5. In the numerical simulation test, the test ends when the post-peak stress is lower than 0.5 MPa. The numerical simulation stress–strain curves of SCS and MCM combined bodies are shown in Figs. 3 and 4, and the test results are shown in Table 6.

From Fig. 3a, when the total rock height ratio is less than or equal to 0.3, the SCS combined body is in the form of single sloped shear failure plane, and the shear plane occurs in the coal. When the total rock height ratios are 0.4 and 0.5, a main shear plane and a secondary shear plane are produced in the coal at the failure of SCS combined body. When the total rock height ratio is 0.6, a main shear plane and two secondary shear planes are produced in the coal at the failure of SCS combined body. When the total rock

Table 5 Combination scheme of SCS and MCM combined bodies

Combination type	Combined body number	Diameter/mm	Total height/mm	Rock–coal–rock height ratio
SCS combined body	SCS1	50	100	5:90:5
	SCS2	50	100	10:80:10
	SCS3	50	100	15:70:15
	SCS4	50	100	20:60:20
	SCS5	50	100	25:50:25
	SCS6	50	100	30:40:30
	SCS7	50	100	35:30:35
	SCS8	50	100	40:20:40
	SCS9	50	100	45:10:45
MCM combined body	MCM1	50	100	5:90:5
	MCM2	50	100	10:80:10
	MCM3	50	100	15:70:15
	MCM4	50	100	20:60:20
	MCM5	50	100	25:50:25
	MCM6	50	100	30:40:30
	MCM7	50	100	35:30:35
	MCM8	50	100	40:20:40
	MCM9	50	100	45:10:45

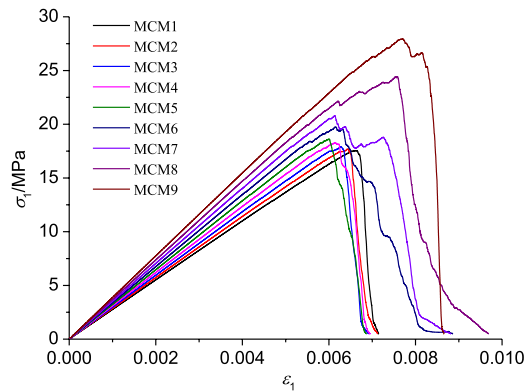**(a)** Axial stress-strain curves

(b) Failure mode

Fig. 3 Numerical simulation results of SCS combined body in conventional uniaxial compression test. **a** Axial stress–strain curves, **b** failure mode

height ratio is 0.7, a main shear plane and several secondary shear planes are produced in the coal at the failure of SCS combined body. When the total rock height ratio is 0.8, there exists no shear failure plane at the failure of SCS combined body, which is manifested as the compression failure of the whole coal. When the total rock height ratio is 0.9, at the failure of SCS combined body, the coal is compressed, and two shear failure planes appear in the bottom sandstone. From Fig. 4a, when the total rock height ratio is less than or equal to 0.4, the MCM combined body is mainly in the form of single sloped shear failure plane. when the total rock height ratio is greater than or equal to 0.5, a main shear plane and a secondary shear planes are produced at the failure of MCM combined body. Because the strength of mudstone is low, the shear failure plane is easy to pass through it. The above shows that the coal–rock height ratio and rock type have a significant influence on the failure mode of coal–rock combined body. For SCS combined body, with the increase of the total rock height ratio, its failure mode changes from single inclined

shear plane to multi inclined shear plane, and then to coal crushing and rock shear plane. For MCM combined body, with the increase of the total rock height ratio, its failure mode changes from single inclined shear plane to multi inclined shear plane, and there exists no compression failure of the whole coal.

3.1 Strength

The relationship between the strength and rock proportion of SCS and MCM combined bodies is shown in Fig. 5. From Fig. 5, under the same rock proportion, the strength of SCS combined body is greater than that of MCM combined body. Besides, with the increase of rock proportion, the strength of SCS and MCM combined bodies increases; and there exists a very good exponential function relationship between the strength and rock proportion ($y_{SCS} = 18.48784 + 0.000067875e^{11.76756x}$, $R^2 = 0.98937$; $y_{MCM} = 17.33661 + 0.11577e^{5.0387x}$, $R^2 = 0.99205$). When the rock proportion is less than or equal to 0.6, the strength difference between SCS
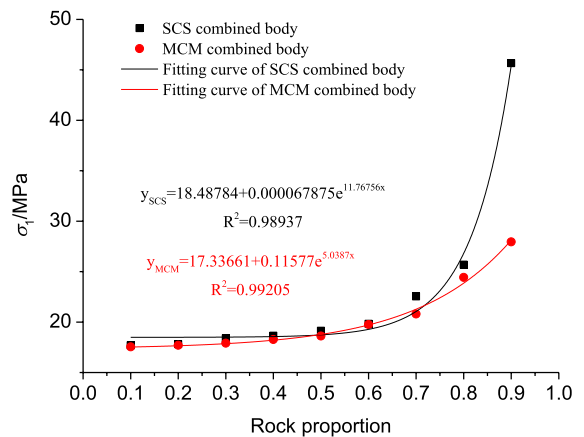
(a) Axial stress-strain curves
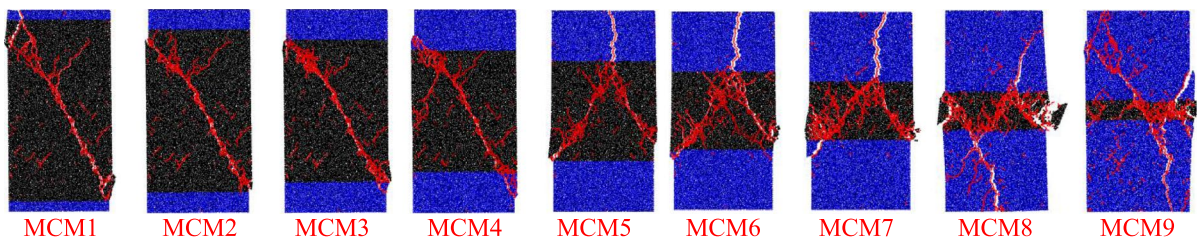
(b) Failure mode

Fig. 4 Numerical simulation results of MCM combined body in conventional uniaxial compression tests. **a** Axial stress–strain curves, **b** failure mode

Table 6 Numerical simulation results of SCS and MCM combined bodies in conventional uniaxial compression test

Specimen number	σ_C/MPa	E/MPa	ε_C/‰
SCS1	17.699	2879.905	6.379
SCS2	17.811	3110.257	5.935
SCS3	18.386	3378.087	5.662
SCS4	18.648	3703.214	5.263
SCS5	19.140	4088.380	4.817
SCS6	19.829	4566.590	4.377
SCS7	22.547	5143.506	4.834
SCS8	25.687	5885.837	5.306
SCS9	45.664	6898.343	8.258
MCM1	17.548	2746.383	6.647
MCM2	17.701	2850.304	6.427
MCM3	17.914	2961.867	6.280
MCM4	18.270	3085.591	6.133
MCM5	18.620	3218.806	6.009
MCM6	19.759	3364.390	6.159
MCM7	20.803	3513.667	6.138
MCM8	24.428	3677.573	7.585
MCM9	27.956	3868.234	7.703

$$y_{SCS}=18.48784+0.000067875e^{11.76756x}$$
$$R^2=0.98937$$

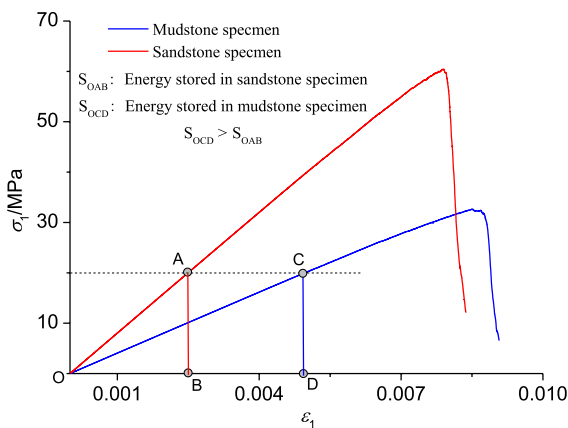$$y_{MCM}=17.33661+0.11577e^{5.0387x}$$
$$R^2=0.99205$$

Fig. 5 Relationship curves between rock proportion and strength of SCS and MCM combined bodies

and MCM combined bodies is very little, and their strength is only slightly higher than that of coal specimen. When the rock proportion is greater than or equal to 0.7, the strength of SCS and MCM combined
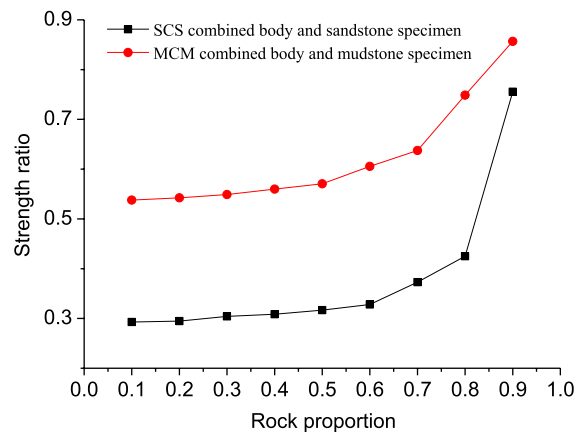
bodies rapidly increases with the increase of rock proportion, and the strength difference between them also increases with the increase of rock proportion.

Through comparing the strength of SCS and MCM combined bodies, it can be concluded that under the same rock proportion, the higher the strength of rock component in combined body, the higher the strength of combined body. The reason is that under the same stress state, coal and rock components have the different stress–strain relationship properties; that is, they have different energy storage characteristics. Under the same rock proportion and stress state, the higher the strength of rock component, the lower the stored energy; on the contrary, the lower the strength of rock component, the higher the stored energy, as shown in Fig. 6. So, the difference of stored energy in different rock components has a significant influence on the strength of combined body. The lower the stored energy in rock components, the higher the strength of combined body; and the higher the stored energy in rock components, the lower the strength of combined body.

The ratio relationship of strength between combined bodies and corresponding rock specimen is shown in Fig. 7. From Fig. 7, under the same rock proportion, the strength ratio of MCM combined body to mudstone specimen is higher than that of SCS combined body to sandstone specimen. For example, when the rock proportion is equal to 0.9, the strength of MCM combined body is 27.956 MPa, which accounts for 85.676% of mudstone specimen strength; and the strength of SCS combined


Fig. 7 Strength ratio curves between combined bodies with different rock proportions and corresponding rock specimens

body is 45.664 MPa, which accounts for 75.548% of sandstone specimen strength. It can be concluded that although the strength of SCS combined body is greater, its speed of approaching the corresponding rock specimen strength is less than that of MCM combined body.
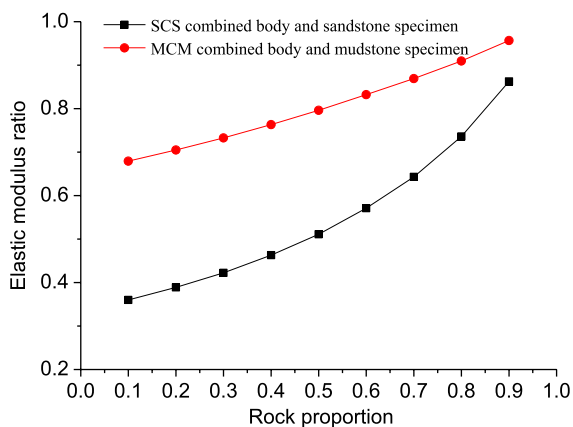
3.2 Elastic Modulus

The relationship between the elastic modulus and rock proportion of SCS and MCM combined bodies is shown in Fig. 8. From Fig. 8, under the same rock proportion, the elastic modulus of SCS combined body is greater than that of MCM combined body. Besides, with the increase

Fig. 6 Comparison of stored energy between sandstone and mudstone specimens
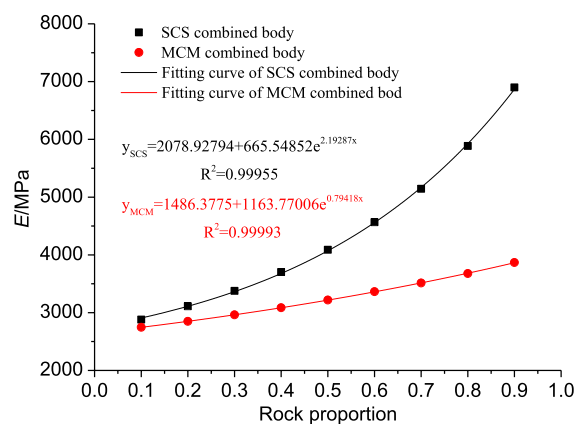
Fig. 8 Relationship curves between rock proportion and elastic modulus of SCS and MCM combined bodies

of rock proportion, the elastic modulus of SCS and MCM combined bodies increases; and there exists a very good exponential function relationship between the elastic modulus and rock proportion $(y_{SCS} = 2078.92794 + 665.54852e^{2.19287x}$, $R^2 = 0.99955$; $y_{MCM} = 1486.3775 + 1163.77006e^{0.79418x}$, $R^2 = 0.99993)$. The difference of elastic modulus between SCS and MCM combined bodies increases with the increase of rock proportion.

The ratio relationship of elastic modulus between combined bodies and corresponding rock specimen is shown in Fig. 9. From Fig. 9, under the same rock proportion, the elastic modulus ratio of MCM combined body to mudstone specimen is higher than that of SCS combined body to sandstone specimen. For example, when the rock proportion is equal to 0.9, the elastic modulus of MCM combined body is 3868.234 MPa, which accounts for 95.679% of mudstone specimen elastic modulus; the elastic modulus of SCS combined body is 6898.343 MPa, which accounts for 86.278% of sandstone specimen elastic modulus. It can be concluded that although the elastic modulus of SCS combined body is greater, its speed of approaching the elastic modulus of corresponding rock specimen is less than that of MCM combined body.
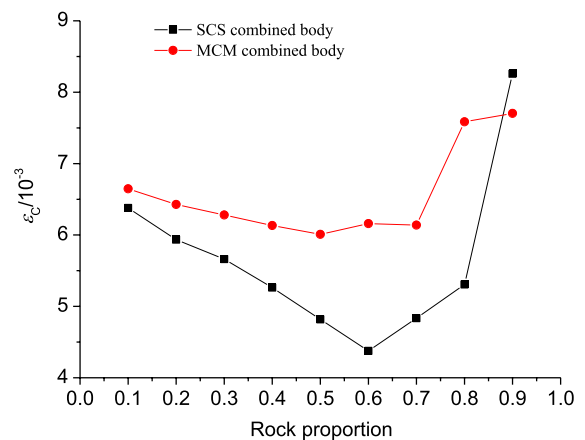
3.3 Peak Axial Strain

The relationship between the peak axial strain and rock proportion of SCS and MCM combined bodies is shown in Fig. 10. From Fig. 10, under the same rock proportion, the peak axial strain of MCM combined body is greater than that of SCS combined body. Besides, the peak axial strain of SCS and MCM combined bodies shows "first decrease, and then increase" evolution law with the increase of rock proportion, and the rock proportion of 0.5 is the obvious turning point of this curve in MCM combined body, the rock proportion of 0.6 is the obvious turning point of this curve in SCS combined body.
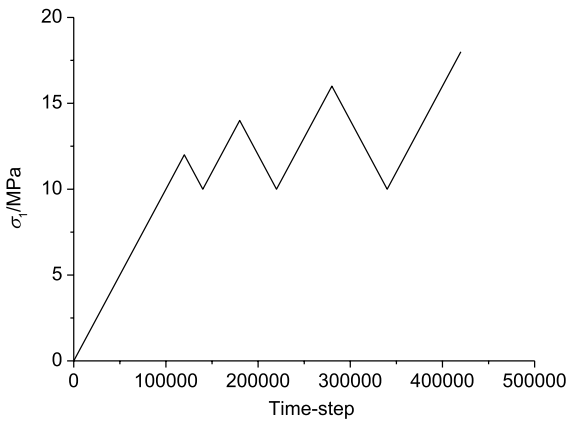
4 Mechanical Properties of Coal–Rock Combined Body in Cyclic Disturbing Loading Test

Based on the conventional uniaxial compression results of SCS and MCM combined bodies, the cyclic disturbing loading simulation test is carried out on these two types of combined bodies. In the numerical simulation test, both the loading rate and unloading rate are chosen as 0.05 m/s, and the stress level increment is set to be 10% of the conventional compression strength. Firstly, combined bodies are loaded to 75% of its conventional uniaxial compression strength, and then unloaded to 10.0 MPa (simulating the static loading in coal measure strata). Then re-loaded to the second level disturbing loading, and then re-unloaded

Fig. 9 Elastic modulus ratio curves between combined bodies with different rock proportions and corresponding rock specimens

Fig. 10 Relationship curves between rock proportion and peak axial strain of SCS and MCM combined bodies

**Fig. 11** The waveform diagram of cyclic disturbing loading

to 10.0 MPa. And so on until the SCS and MCM combined bodies is completely destroyed. The waveform diagram of cyclic disturbing loading is shown in Fig. 11. When the post-peak stress is lower than 0.5 MPa, the test is over.

4.1 Stress–Strain Curve

The stress–strain curves of SCS and MCM combined body in conventional uniaxial compression and cyclic disturbing loading tests are shown in Figs. 12 and 13. From Fig. 12, when the rock proportion is less than or equal to 0.3, the shape of stress–strain curve of SCS combined body in conventional uniaxial compression and cyclic disturbing loading tests has a good
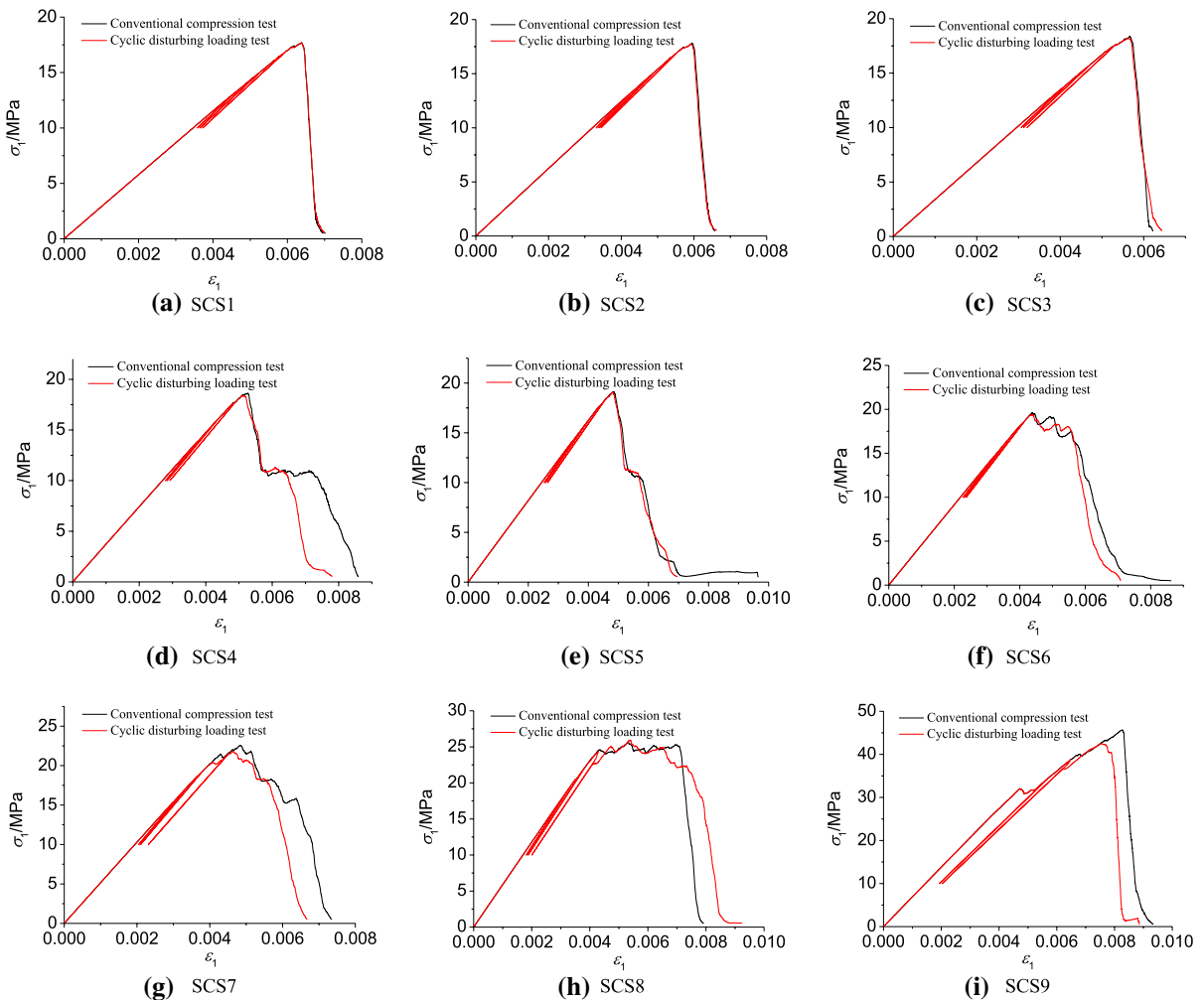
Fig. 12 Numerical simulation stress–strain curves of SCS combined body in conventional uniaxial compression and cyclic disturbing loading tests
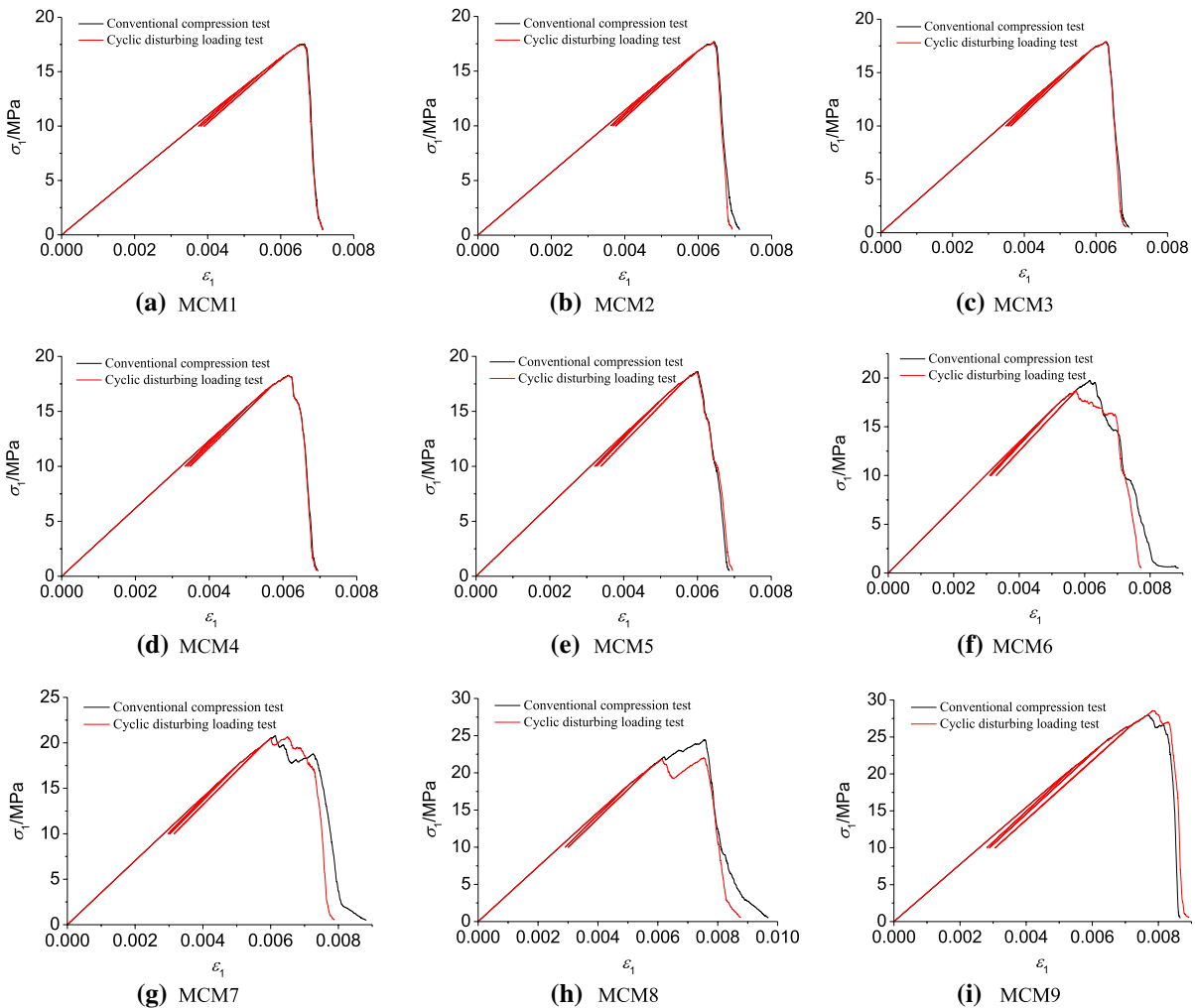
Fig. 13 Numerical simulation stress–strain curves of MCM combined body in conventional uniaxial compression and cyclic disturbing loading tests

coincidence. When the rock proportion is from 0.4 to 0.6, the shape of pre-peak stress–strain curve of SCS combined body in conventional uniaxial compression and cyclic disturbing loading tests has a good coincidence, but the shape of post-peak stress–strain curve has a big change obviously. When the rock proportion is greater than or equal to 0.7, the shape of pre-peak and post-peak stress–strain curves of SCS combined body in conventional uniaxial compression and cyclic disturbing loading tests also changes obviously.

From Fig. 13, when the rock proportion is less than or equal to 0.5, the shape of stress–strain curve of MCM combined body in conventional uniaxial compression and cyclic disturbing loading tests has

a good coincidence. When the rock proportion is greater than or equal to 0.6, the shape of pre-peak and post-peak stress–strain curves of MCM combined body in conventional uniaxial compression and cyclic disturbing loading tests changes obviously.

By comparing Figs. 12 and 13, it can be concluded that the shape change of stress–strain curve of SCS combined body in conventional uniaxial compression and cyclic disturbing loading tests is greater than that of MCM combined body. That is, under the conventional uniaxial compression and cyclic disturbing loading, if the higher the strength of rock component in coal–rock combined body, the more obvious the shape difference of the two stress–strain curves.

4.2 Strength

The strength comparison of SCS and MCM combined bodies in conventional uniaxial compression and cyclic disturbing loading tests is shown in Table 7 and Fig. 14. From Table 7, under the same rock proportion, the strength of SCS combined body in cyclic disturbing loading test is greater than that of MCM combined body. From Table 7 and Fig. 14, in the nine kinds of sandstone proportion schemes, only when the sandstone proportion is 0.8, the strength of SCS combined body in cyclic disturbing loading tests is greater than its conventional compression strength. In the nine kinds of mudstone proportion schemes, when the mudstone proportion is 0.4 and 0.9, the strength of MCM combined body in cyclic disturbing loading tests is greater than its conventional compression strength. Besides, with the increase of rock proportion, the strength of SCS and MCM combined bodies increases; and there also exists a very good exponential function relationship between the strength and rock proportion ($y_{SCS} = 18.2297 + 0.00173e^{10.60649x}$,

Table 7 Strength comparison of SCS and MCM combined bodies in conventional uniaxial compression and cyclic disturbing loading tests

Specimen number	σ_C/MPa		Error/%
	Conventional uniaxial compression test	Cyclic disturbing loading test	
SCS1	17.699	17.682	− 0.096
SCS2	17.811	17.724	− 0.488
SCS3	18.386	18.271	− 0.625
SCS4	18.648	18.388	− 1.394
SCS5	19.140	19.122	− 0.094
SCS6	19.829	19.599	− 1.160
SCS7	22.547	21.813	− 3.055
SCS8	25.687	25.930	0.946
SCS9	45.664	42.584	− 6.745
MCM1	17.548	17.501	− 0.268
MCM2	17.701	17.635	− 0.373
MCM3	17.914	17.866	− 0.268
MCM4	18.270	18.291	0.115
MCM5	18.620	18.544	− 0.408
MCM6	19.759	18.777	− 4.970
MCM7	20.803	20.682	− 0.582
MCM8	24.428	22.024	− 0.984
MCM9	27.956	28.579	2.229

(a) SCS combined body
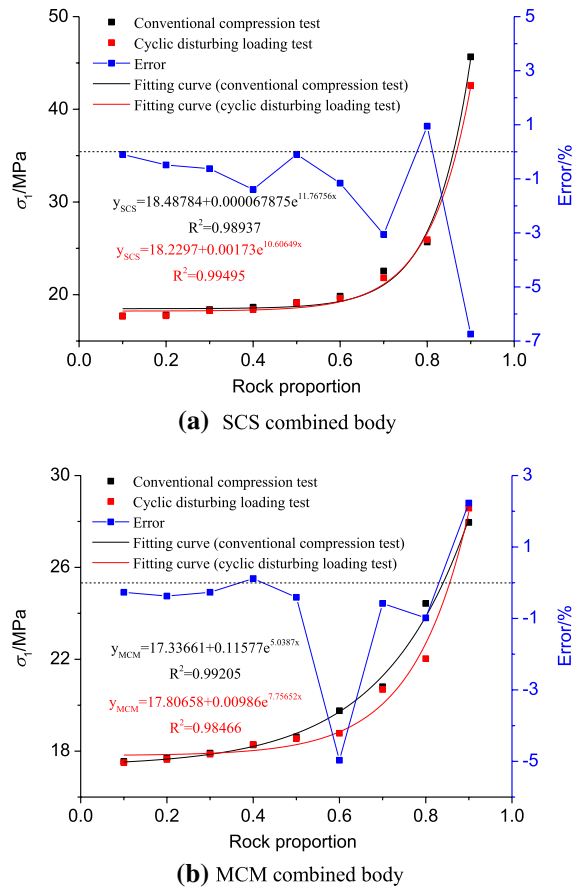
(b) MCM combined body

Fig. 14 Strength comparison of SCS and MCM combined bodies in conventional uniaxial compression and cyclic disturbing loading tests

$R^2 = 0.99495$; $y_{MCM} = 17.80658 + 0.00986e^{7.75652x}$, $R^2 = 0.98466$).

Through the above analysis, it can be concluded that the cyclic disturbing loading has two effects on the coal–rock combined bodies, namely: plastic softening and plastic strengthening effects. Which kind of effect will play a dominant role is related to the deformation, dislocation and defect evolution of coal–rock combined body during the load-unloading process. The plastic softening effect makes the cracks and defects in coal–rock combined body develop further, so as to reduce its strength; and the plastic hardening effect limits the development of these cracks and defects, so as to improve its strength. The mutual restriction and competition of these two effects will determine the final strength of coal–rock combined body.
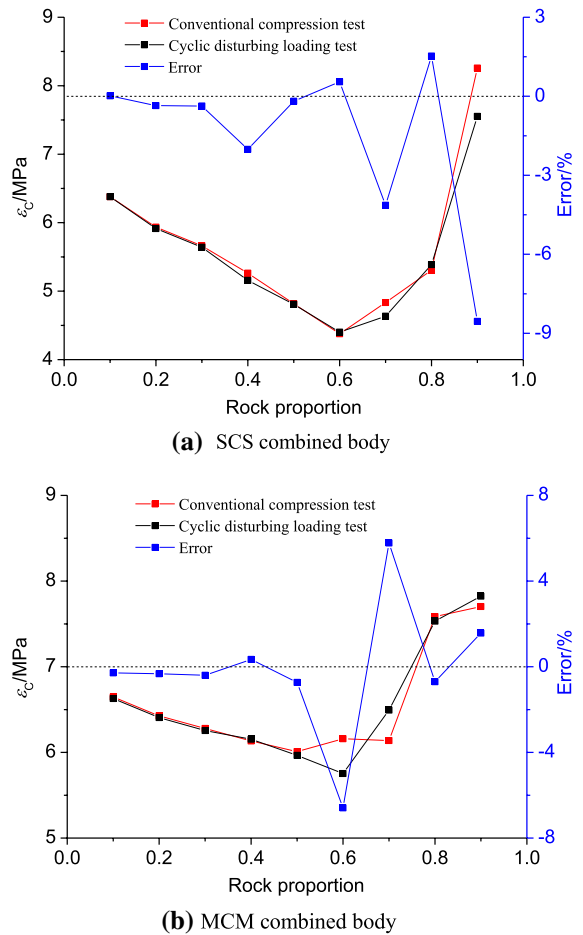
4.3 Peak Axial Strain

The peak axial strain of SCS and MCM combined bodies in conventional uniaxial compression and cyclic disturbing loading tests is shown in Table 8 and Fig. 15.

From Table 8 and Fig. 15, compared with the results in conventional compression test, when the sandstone proportion is 0.1, 0.6 and 0.8, the peak axial strain of SCS combined body in cyclic disturbing loading test increases; when the mudstone proportion is 0.4, 0.7 and 0.9, the peak axial strain of MCM combined body in cyclic disturbing loading test increases. Besides, the peak axial strain of the two combined bodies in cyclic disturbing loading test shows the evolution characteristics of "first decreasing and then increasing" with the increase of rock proportion, and the rock proportion of 0.6 is the turning point of peak axial strain of the two combined bodies.

Table 8 Peak Axial strain comparison of rock-coal combined bodies in conventional uniaxial compression and cyclic disturbing loading tests

Specimen number	$\varepsilon_C/‰$		Error/%
	Conventional uniaxial compression test	Cyclic disturbing loading test	
SCS1	6.379	6.380	0.016
SCS2	5.935	5.914	− 0.354
SCS3	5.662	5.641	− 0.371
SCS4	5.263	5.157	− 2.014
SCS5	4.817	4.808	− 0.187
SCS6	4.377	4.401	0.548
SCS7	4.834	4.634	− 4.137
SCS8	5.306	5.387	1.527
SCS9	8.258	7.552	− 8.549
MCM1	6.647	6.628	− 0.286
MCM2	6.427	6.406	− 0.327
MCM3	6.280	6.255	− 0.398
MCM4	6.133	6.154	0.342
MCM5	6.009	5.965	− 0.732
MCM6	6.159	5.753	− 6.592
MCM7	6.138	6.494	5.780
MCM8	7.585	7.532	− 0.699
MCM9	7.703	7.824	1.571

(a) SCS combined body

(b) MCM combined body

Fig. 15 Peak axial strain comparison of SCS and MCM combined bodies in conventional uniaxial compression and cyclic disturbing loading tests

4.4 Elastic Modulus and Irreversible Axial Strain

The elastic modulus and irreversible strain of SCS and MCM combined bodies in cyclic disturbing loading tests is shown in Tables 9 and 10, Figs. 16 and 17. Here, the elastic modulus refers to the secant elastic modulus in the loading phase between the pre-static loading (10 MPa) and the point corresponding to 75% of the conventional compression strength.

From Table 9, under the same loading number, the elastic modulus of SCS and MCM combined bodies increases with the increase of rock proportion. When the rock proportion is the same, the elastic modulus of SCS combined body is greater than that of MCM combined body under the same loading number. From Table 10, under the same loading number, there

Table 9 Elastic modulus of SCS and MCM combined bodies in cyclic disturbing loading test

Specimen number	Loading number			
	1	2	3	4
SCS1	2819.240	3114.605	3112.236	3101.620
SCS2	3049.629	3357.903	3354.787	3345.895
SCS3	3302.854	3638.411	3635.717	3615.582
SCS4	3624.953	3984.732	3986.723	3962.135
SCS5	4028.389	4392.435	4392.988	4369.962
SCS6	4505.801	4897.373	4901.542	4880.620
SCS7	5076.008	5496.785	5476.391	5271.928
SCS8	5821.964	6269.492	6235.727	6066.129
SCS9	5745.933	6490.425	6378.812	–
MCM1	2680.189	2976.264	2975.405	2965.052
MCM2	2787.518	3084.988	3084.568	3074.155
MCM3	2899.319	3202.041	3201.829	3189.955
MCM4	3029.792	3333.576	3333.710	3321.126
MCM5	3163.666	3472.481	3476.579	3447.088
MCM6	3315.436	3623.372	3626.944	3593.178
MCM7	3471.142	3779.394	3781.794	3747.252
MCM8	3618.368	3937.657	3912.041	–
MCM9	3810.358	4129.173	4119.442	4042.638

Table 10 Irreversible strain of SCS and MCM combined bodies in cyclic disturbing loading test

Specimen number	Loading number		
	1	2	3
SCS1	110.088	68.154	76.566
SCS2	99.637	65.863	66.418
SCS3	107.775	57.809	82.453
SCS4	97.118	42.171	88.261
SCS5	89.188	42.317	62.183
SCS6	84.050	31.936	59.603
SCS7	104.186	54.700	212.282
SCS8	114.082	61.803	129.448
SCS9	485.692	92.088	–
MCM1	112.611	72.720	80.723
MCM2	116.336	65.411	73.558
MCM3	112.604	65.449	77.364
MCM4	112.415	61.645	73.600
MCM5	112.265	50.459	114.185
MCM6	125.975	42.064	161.032
MCM7	132.984	48.661	126.984
MCM8	188.349	104.144	–
MCM9	226.261	82.750	167.618

is no obvious law between irreversible strain and rock proportion. In this paper, the irreversible strain refers to the difference of axial strain at the valley stress of two adjacent loading cycles.

From Figs. 16 and 17, the elastic modulus of SCS and MCM combined bodies in the last disturbing loading cycle is less than that in the previous cycle. Except that No. SCS9 and No. MCM8 combined bodies failed at the third disturbing loading cycle, other combined bodies with different rock proportions failed at the fourth disturbing loading cycle, and the irreversible strain caused by the penultimate disturbing loading cycle is greater than that of the previous cycle. That is, in the process of cyclic disturbing loading with the same stress increment, when the irreversible strain increases at the end of a disturbing loading cycle and the elastic modulus decreases in the next disturbing loading phase, it indicates that the combined body is about to be destroyed.

4.5 Crack Evolution and Acoustic Emission Characteristics

4.5.1 Crack Evolution

The crack evolution characteristics of SCS and MCM combined bodies in cyclic disturbing loading tests is shown in Figs. 18 and 19.

From Figs. 18 and 19, in the process of cyclic disturbing loading, the shear cracks of SCS and MCM combined bodies show the characteristics of "multi-step" growth, and the number of shear cracks is greater than that of tensile cracks. Besides, the "multi-step" growth characteristics of tensile cracks are not obvious, and the time point of rapid increase of tensile cracks obviously lags behind that of shear cracks. Although both of the shear crack and tensile crack have a rapid growth before approaching failure, this feature of tensile crack is more obvious. So, the rapid growth of tensile crack can be used as a failure precursor of coal–rock combined body. Moreover, the internal cracks of coal-rock combined body has not formed the dominant fracture surface through the whole specimen at the peak stress point of the last disturbing loading cycle. It shows that the coal-rock combined body is not damaged at this time, and its failure occurs at a certain point of the post-peak phase. But, it should be noted that there is no significant difference in the failure modes of SCS and MCM
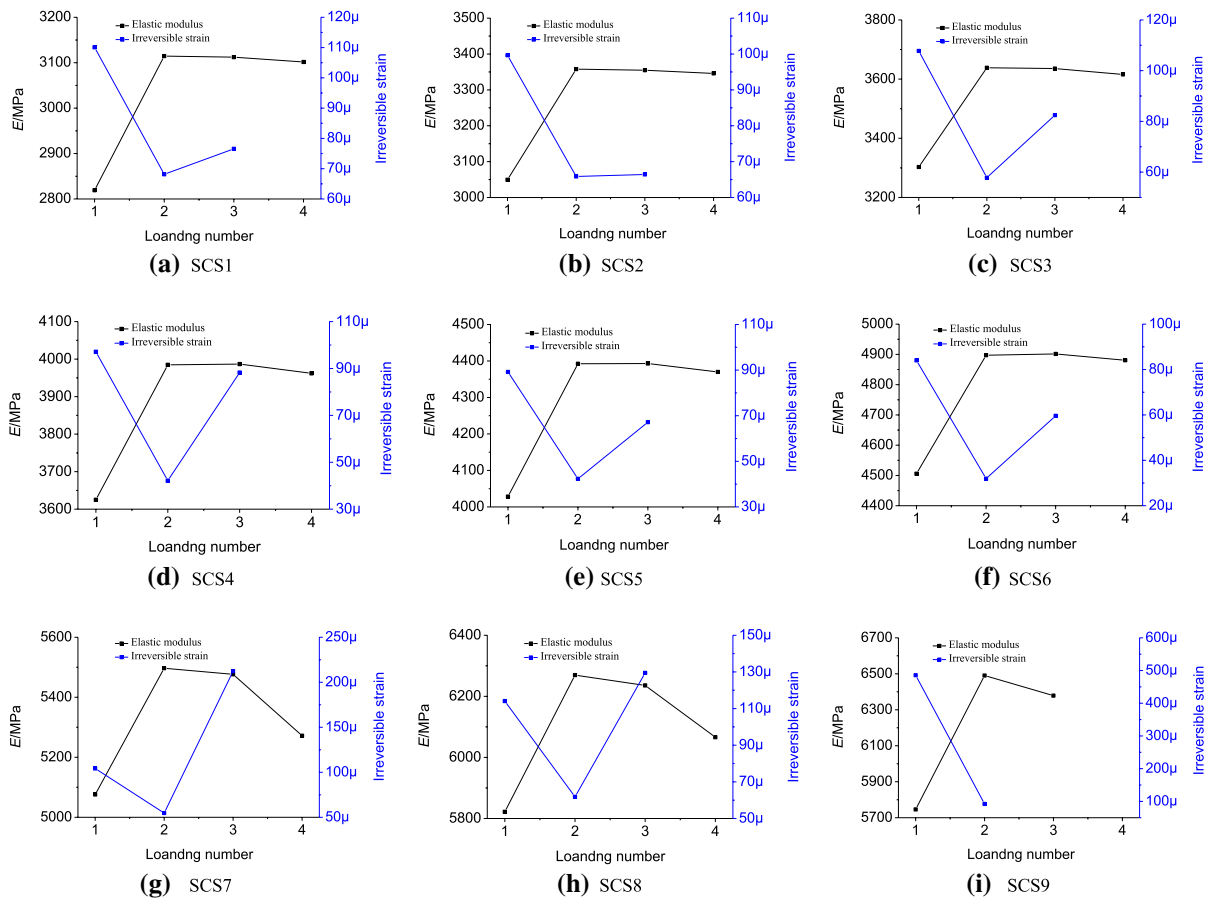
Fig. 16 Elastic modulus and irreversible strain of SCS combined body in cyclic disturbing loading test

combined bodies under the conventional uniaxial compression and cyclic disturbing loading.

4.5.2 AE Hit Count

In the lab rock mechanics test, there are two kinds of AE signals, namely: fracture-typed and friction-typed signals. If there occur the very strong friction-typed AE signals, it will affect the accuracy of research results on the regularity of rock AE activity. In the numerical simulation test, the initiated cracks in specimen are monitored and recorded by the Fish program of PFC, which effectively eliminates the discreteness of the specimen and the influence of friction-typed AE signals in the lab test, and can accurately obtain the AE activity law of specimen with loading. In the lab rock mechanics test, the each propagation of cracks corresponds to an AE hit. So, in the numerical simulation test, the counting number of new cracks according to the same time-step interval can be approximately equivalent to the measurement of AE hit, and then the research on the AE activity law of loaded coal–rock combined body is realized.

The axial stress and AE hit count of SCS and MCM combined bodies in cyclic disturbing loading tests are shown in Figs. 20 and 21, and the evolution curve of maximum AE hit count with rock proportion is shown in Fig. 22. It should be noted that the AE hit counts was counted every 3000 time-steps.
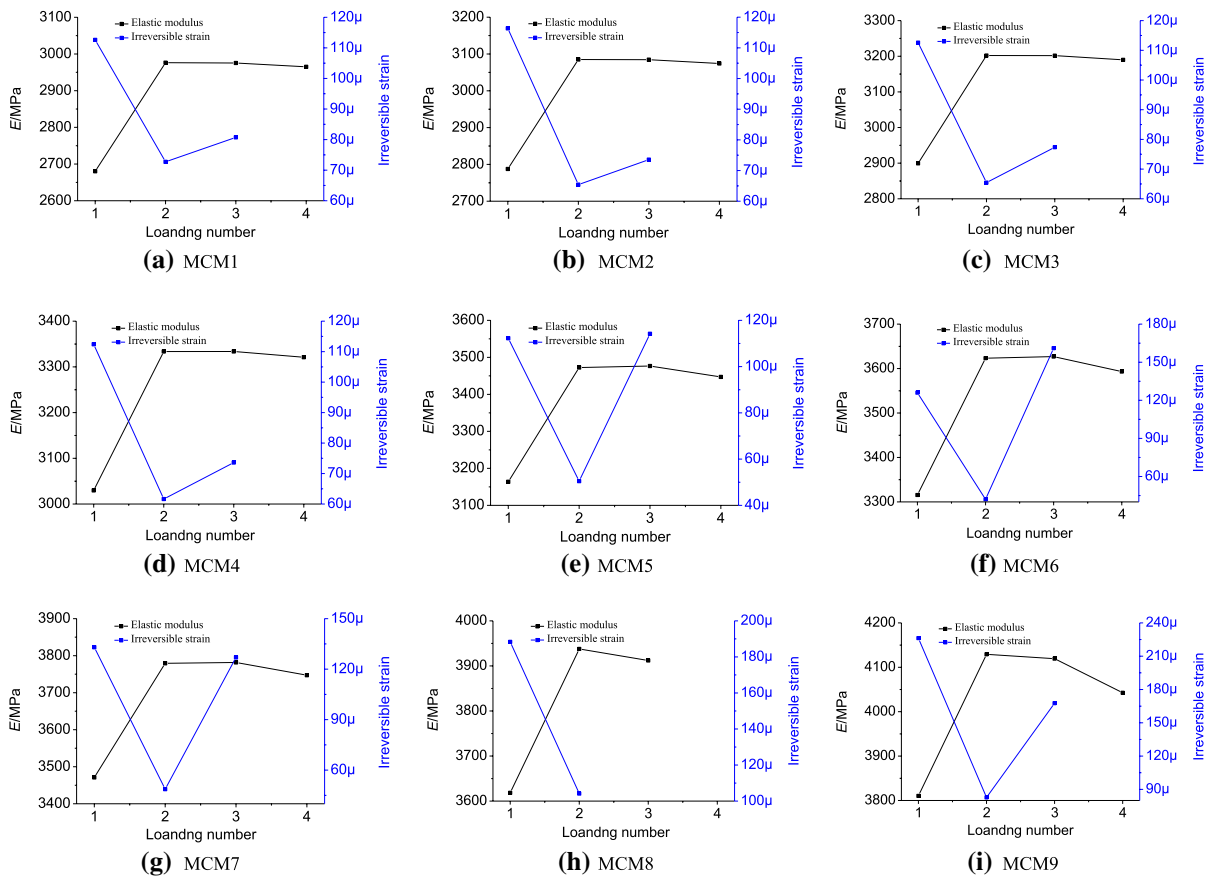
Fig. 17 Elastic modulus and irreversible strain of MCM combined body in cyclic disturbing loading test

From Fig. 20, the maximum AE hit count of SCS combined bodies lags behind the peak stress point. When the rock proportion is less than or equal to 0.3, the AE hit count in the post-peak phase of SCS combined body are greater than 350; when the rock proportion is from 0.4 to 0.8, the AE hit count decreases significantly, and all are lower than 240; when the rock proportion is equal to 0.9, the AE hit count is greater than 300, showing the characteristics of increasing. The above shows that the maximum AE hit count of SCS combined body presents the characteristics of "big at both ends and small in the middle" with the increase of rock proportion.

From Fig. 21, the maximum AE hit count of MCM combined bodies also lags behind the peak stress point. When the rock proportion is less than or equal to 0.3, the AE hit count in the post-peak phase of MCM combined body are greater than 400; when the rock proportion is from 0.4 to 0.8, the AE hit count decreases significantly, and all are lower than 400; when the rock proportion is equal to 0.9, the AE hit count is greater than 400, showing the characteristics of increasing. The above shows that the maximum AE hit count of MCM combined body also presents the characteristics of "big at both ends and small in the middle" with the increase of rock proportion.

From Figs. 20 and 21, the maximum AE hit count of SCS and MCM combined bodies lags behind the peak stress point, that is, the failure of the combined body occurs at a certain point of the post-peak phase. When the rock proportion is less than or equal to 0.3, the duration of AE activities in the post-peak phase
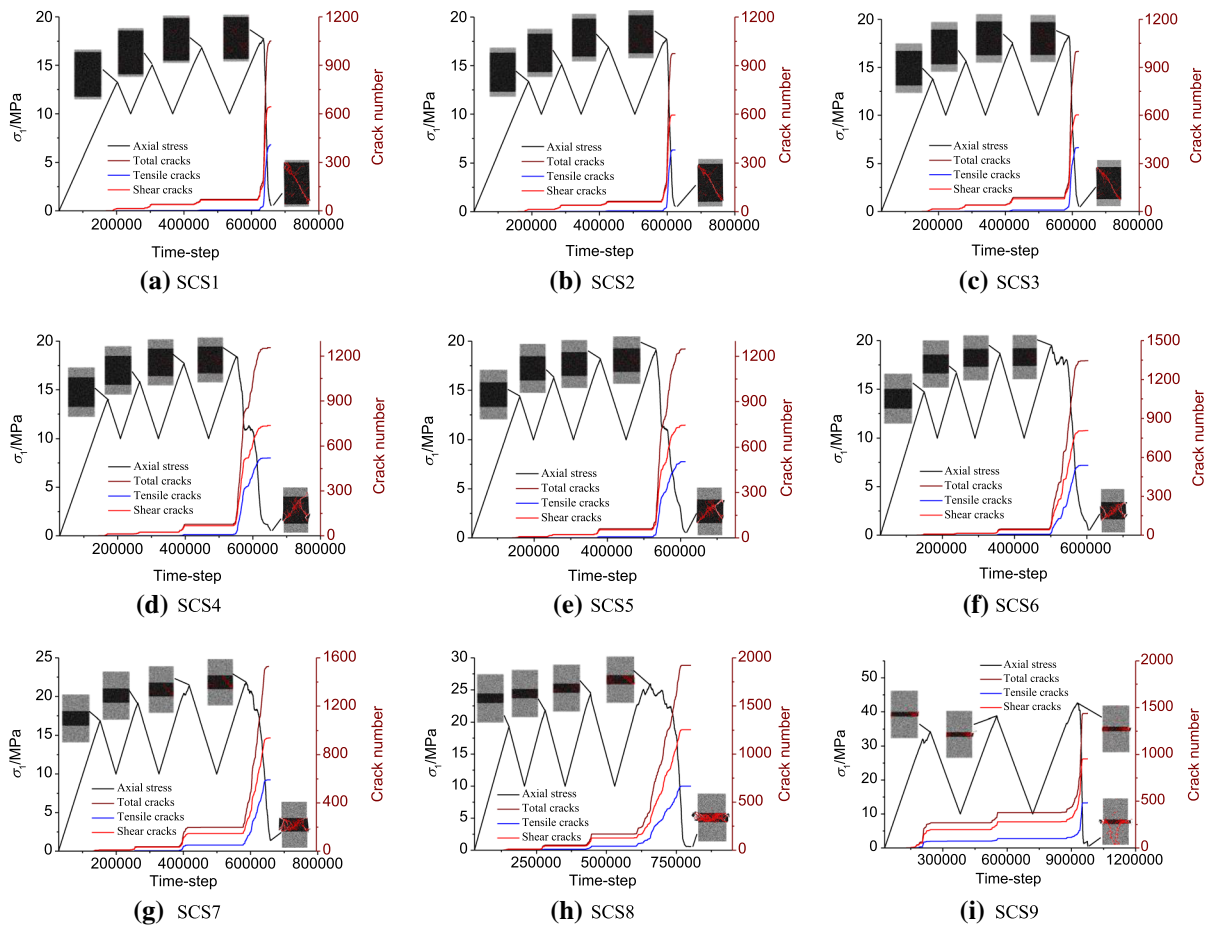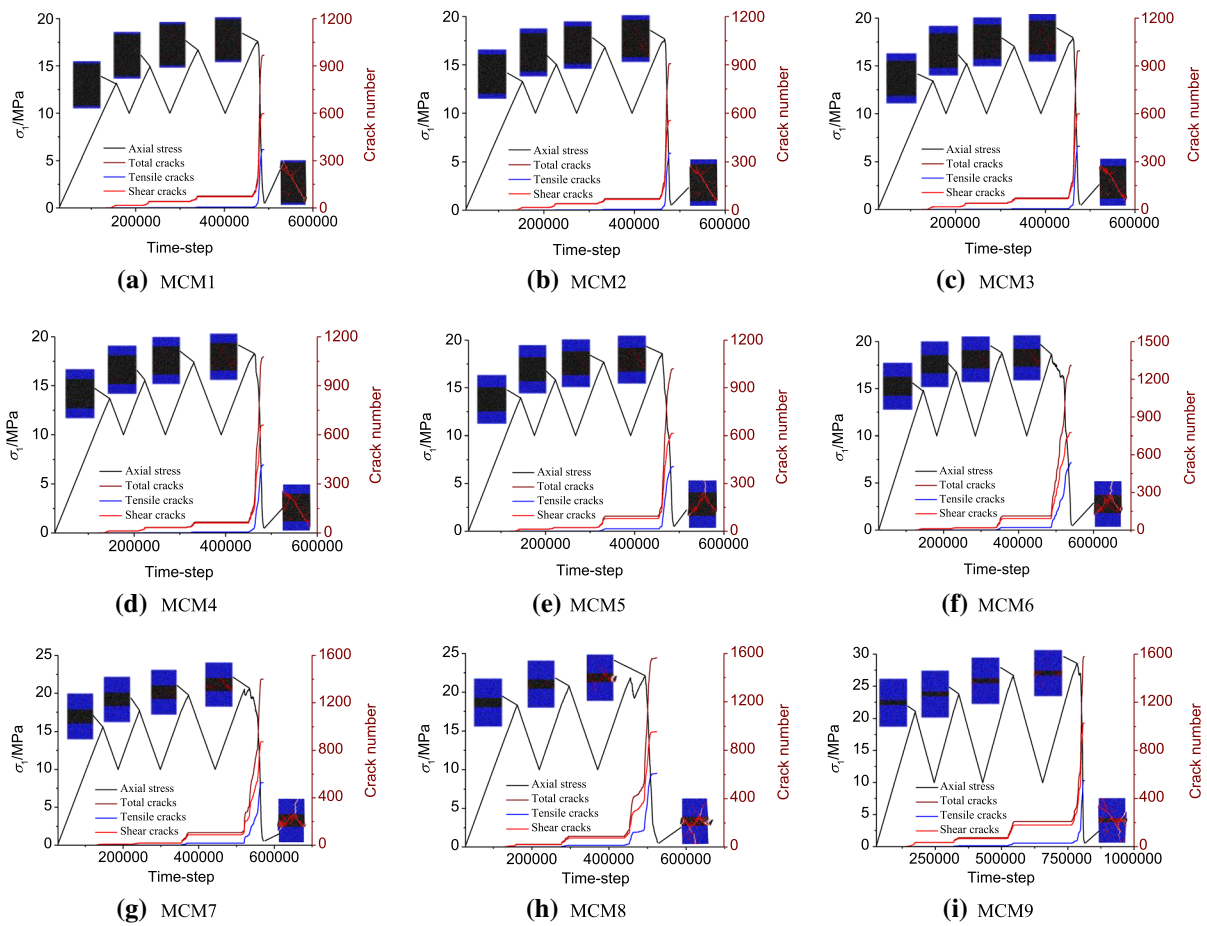
Fig. 18 Crack evolution characteristics of SCS combined body in cyclic disturbing loading test

of combined body is relatively short; when the rock proportion is from 0.4 to 0.8, the duration of AE activities in the post-peak phase of combined body increases significantly; when the rock proportion is equal to 0.9, the duration of AE activities in the post-peak phase of combined body begins to decrease.

From Fig. 22, under the same rock proportion, the maximum AE hit count of MCM combined body is greater than that of SCS combined body. This is because the strength of mudstone component in MCM combined body is lower than that of sandstone component in SCS combined body. Besides, the maximum AE hit count of SCS and MCM combined bodies presents the characteristics of "big at both ends and small in the middle"

with the increase of rock proportion. The reason is that when the rock proportion is relatively small, the shape of stress–strain curve of SCS and MCM combined bodies is similar to that of coal specimen, and the axial stress decreases rapidly in the post-peak phase, indicating that the failure process of the two combined bodies is relatively fast. When the rock proportion is very large, the axial stress of SCS and MCM combined bodies also decreases rapidly in the post-peak phase, which also shows that the failure process of the two combined bodies is also relatively fast. When the rock proportion is in the middle, the axial stress of SCS and MCM combined bodies decreases slowly in the post-peak phase, indicating that the failure process of the two

Fig. 19 Crack evolution characteristics of MCM combined body in cyclic disturbing loading test

combined bodies is relatively slow-motion. These show that the fast failure process often causes the strong AE activities, while the slow-motion failure process presents the low AE activities. So, from the perspective of preventing coal mine rockburst, it is beneficial to adopt different methods to change the mechanical properties of coal and rock masses, especially improve its plastic deformation characteristics in the post-peak phase.

5 Conclusions

In this work, The mechanical properties of SCS and MCM combined body are deeply studied by numerical simulation method. Through the in-depth analysis

of the data, the following main innovative conclusions are obtained.

(1) Under the same rock proportion, the strength and elastic modulus of SCS combined body in conventional uniaxial compression test are greater than that of MCM combined body; and their strength and elastic modulus increase exponentially with the increase of rock proportion.

(2) In the conventional uniaxial compression and cyclic disturbing loading tests, with the increase of rock proportion, the difference of stress–strain curve shape of SCS and MCM
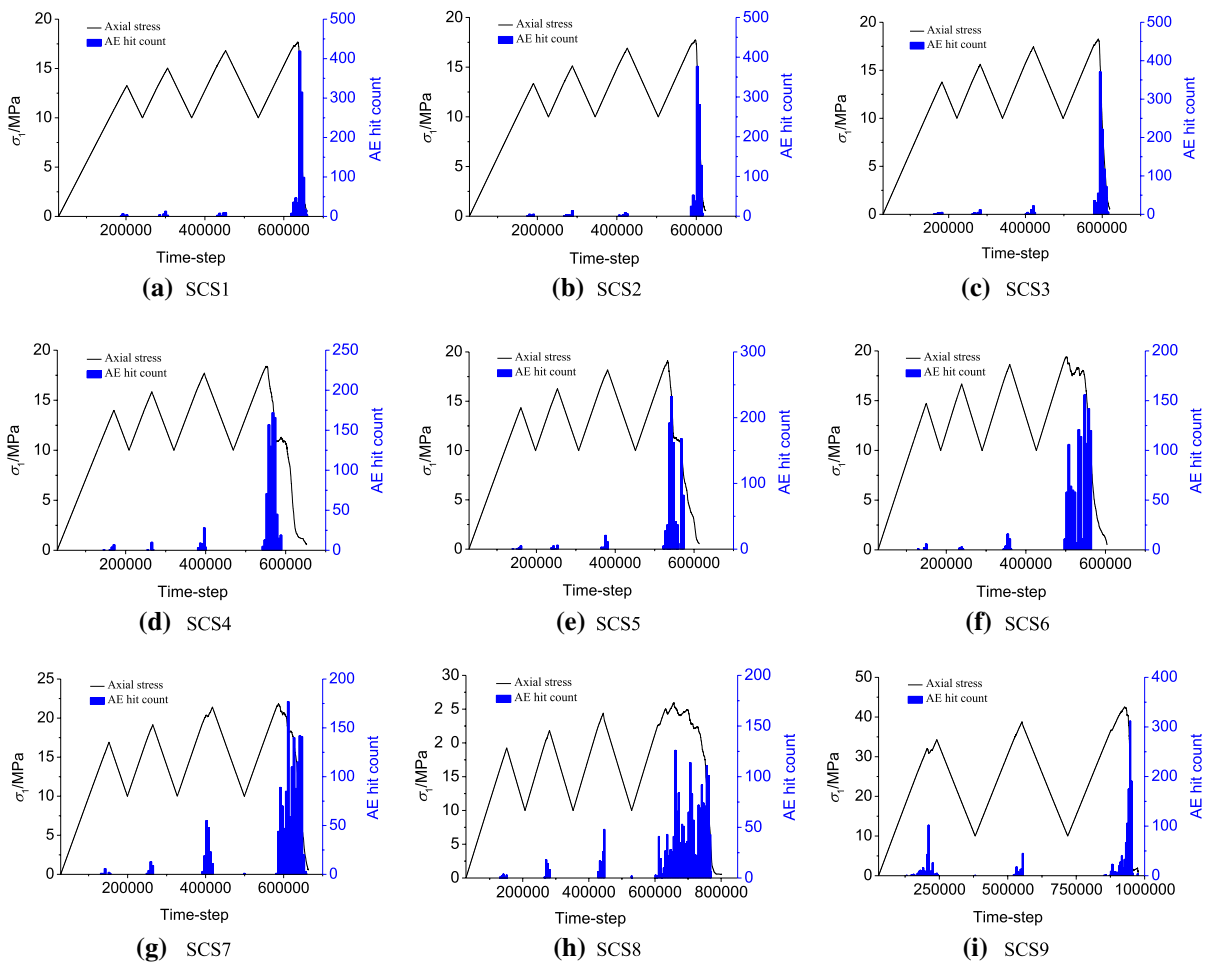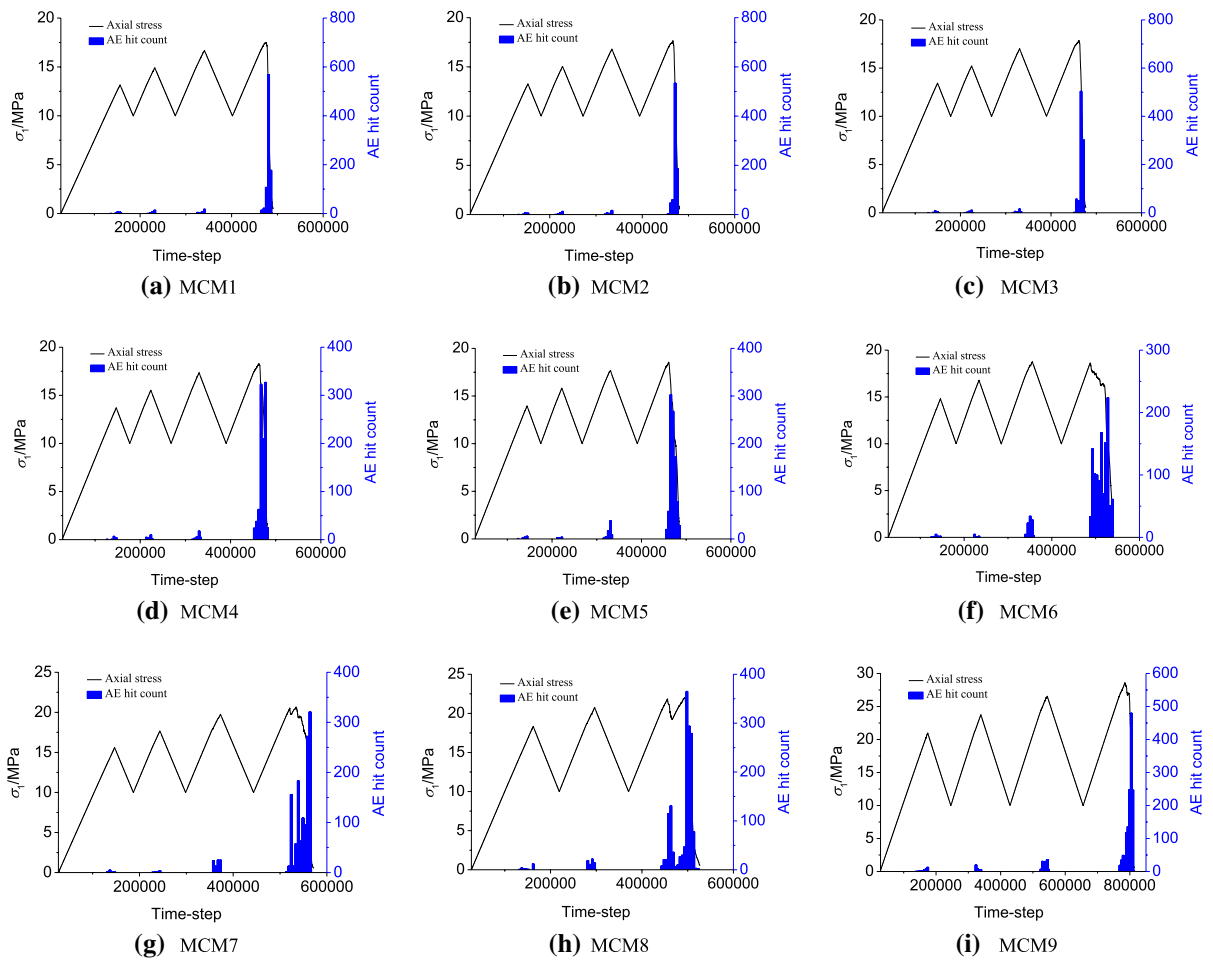
Fig. 20 Acoustic emission characteristics of SCS combined body in cyclic disturbing loading test

combined bodies increases, and the peak axial strain of SCS and MCM combined bodies shows the evolution characteristics of "first decreasing and then increasing".

(3) Under the same rock proportion, the strength of SCS combined body in cyclic disturbing loading test is greater than that of MCM combined body; and their strength increases exponentially with the increase of rock proportion.

(4) The cyclic disturbing loading has two effects on the SCS and MCM combined bodies, namely: plastic softening and plastic strengthening effects. Which kind of effect will play

a dominant role is related to the deformation, dislocation and defect evolution of the combined body during the load-unloading process. The mutual restriction and competition of these two effects will determine the final strength of combined body.

(5) Under the same rock proportion, the maximum AE hit count of MCM combined body is greater than that of SCS combined body, and the maximum AE hit count of SCS and MCM combined bodies presents the characteristics of "big at both ends and small in the middle" with the increase of rock proportion.

Fig. 21 Acoustic emission characteristics of MCM combined body in cyclic disturbing loading test
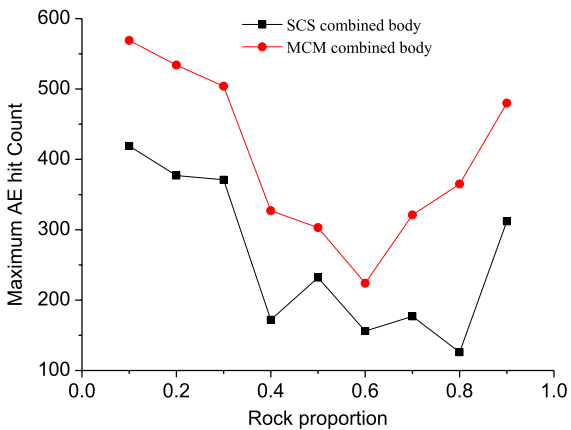
Fig. 22 Relation between maximum AE hit count and rock proportion of SCS and MCM combined bodies

Availability of Data and Materials All relevant data used to support the findings of this study are included within the article, and also available from the corresponding author upon request.

Code Availability Data that support the findings of this study can be gained from the corresponding author upon request.

Declarations

Conflict of interest The authors declare that they have no conflict of interest.

References

Chen M, Yang SQ, Zhang YC, Zang CW (2016) Analysis of the failure mechanism and support technology for the dongtan deep coal roadway. Geomech Eng 11(3):401–420

Chen SJ, Ge Y, Yin DW, Yang HS (2019) An experimental study of the uniaxial failure behaviour of rock-coal composite samples with pre-existing cracks in the coal. Adv Civ Eng, Article ID 8397598, 12 pp

Chen ZB, Li LH, Zhang YN (2020) Laboratory investigation of the mechanical properties of coal–rock combined body. Bull Eng Geol Environ 79(4):1947–1958

Chen YL, Zuo JP, Liu DJ, Li YJ, Wang ZB (2021) Experimental and numerical study of coal–rock bimaterial composite bodies under triaxial compression. Int J Coal Sci Technol 8(5):908–924

Gao FQ, Kang HP, Yang L (2020) Experimental and numerical investigations on the failure processes and mechanisms of composite coal–rock specimens. Sci Rep 10(1):13422

Gao BB, Ren CN, Dong Q, Chen LW (2021) Study on dynamic behavior law and microseismic monitoring in stoping process of roadway with high gas and wide coal pillar. Shock Vib, Article ID 5135964, 14 pp

He YC, Zhao PX, Li SG, Ho CH, Zhu ST, Kong XG, Barbieri DM (2021a) Mechanical properties and energy dissipation characteristics of coal–rock-like composite materials subjected to different rock-coal strength ratios. Nat Resour Res 30(3):2179–2193

He ZL, Lu CP, Zhang XF, Wang C, Wang BQ, Zhou T (2021b) Numerical and field investigations on rockburst risk adjacent to irregular coal pillars and fault. Shock Vib, Article ID 8830899, 17 pp

Li XL, Cao ZY, Xu YL (2020) Characteristics and trends of coal mine safety development. Energy Sources Part A Recov Util Environ Eff. https://doi.org/10.1080/15567036.2020.1852339

Li A, Ji BN, Ma Q, Liu CY, Wang F, Ma L, Mu PF, Mou L, Yang YX, Ding XS (2021) Design of longwall coal pillar for the prevention of water inrush from the seam floor with through fault. Geofluids, Article ID 5536235, 14 pp

Liu HL, Wang PT, Yang TH, Xu T, Yu QL, Xia D (2015) Mechanical characteristics of granite under uniaxial compressive and ae monitoring test using particle flow code. J China Coal Soc 40(8):1790–1795

Liu JW, Wu N, Si GY, Zhao MX (2021) Experimental study on mechanical properties and failure behaviour of the pre-cracked coal–rock combination. Bull Eng Geol Environ 80(3):2307–2321

Lu ZG, Ju WJ, Gao FQ, Yi K (2021) Influence of loading rate on the failure characteristics of composite coal–rock specimens under quasi-static loading conditions. Rock Mech Rock Eng. https://doi.org/10.1007/s00603-021-02699-2

Luo B, Sun YJ, Xu ZM, Chen G, Zhang L, Lu WN, Zhao XM, Yuan HQ (2021) Damage characteristics and mechanism of the 2017 groundwater inrush accident that occurred at Dongyu Coalmine in Taiyuan, Shanxi, China. Water, Article ID 368, 12 pp

Mu K, Li TB, Yu J, Cai YY, Liu SY, Tu BX, Jiang HC (2014) Mesoscopic simulation of relationship of acoustic emission and compressive deformation behavior in sandstone under confining pressures effect. Chin J Rock Mech Eng 33(S1):2786–2793

Pan B, Yu WJ, Shen WB (2021) Experimental study on energy evolution and failure characteristics of rock–coal–rock combination with different height ratios. Geotech Geol Eng 39(1):425–435

Van der Merwe JN (2006) South African coal pillar database. J S Afr Inst Min Metall 106(2):115–128

Xin HQ, Li QH, Liu L, Liu ZJ, Hou JM (2021) Analysis on the influence of fault protection coal pillar size on rockburst. Geofluids, Article ID 5563347, 11 pp

Xue JH, Chen ZH, Li YH, Wang JY, Li X (2022) Failure characteristics of coal–rock combined bodies based on acoustic emission signals. Arab J Geosci 15(2), Article ID 135

Yang YJ, Zhao NN, Ma DP, Zhang FJ (2016) Study on stability of strip coal pillar with different moisture content. J Min Saf Eng 33(1):42–48

Yang L, Gao FQ, Wang XQ, Li JZ (2019) Energy evolution law and failure mechanism of coal–rock combined specimen. J China Coal Soc 44(12):3894–3902

Yang L, Gao FQ, Wang XQ (2020) Mechanical response and energy partition evolution of coal–rock combinations with different strength ratios. Chin J Rock Mech Eng 39(S2):3297–3305

Zhang YL (2014) Numerical simulation study on the landslide process and impact disaster. M.S. Thesis. Hohai University, Nanjing, China

Zhang HW, Elsworth D, Wang ZJ (2018) Failure response of composite rock-coal samples. Geomech Geophys Geo-Energy Geo-Resour 4(2):175–192